A&A, 696, A87 (2025)
https://doi.org/10.1051/0004-6361/202452451

Astronomy & Astrophysics

The eventful life of a luminous galaxy at $z = 14$: metal enrichment, feedback, and low gas fraction?

Stefano Carniani[1], Francesco D'Eugenio[2,3,4], Xihan Ji[2,3], Eleonora Parlanti[1], Jan Scholtz[2,3], Fengwu Sun[5], Giacomo Venturi[1], Tom J. L. C. Bakx[6], Mirko Curti[7], Roberto Maiolino[2,3,8], Sandro Tacchella[2,3], Jorge A. Zavala[9], Kevin Hainline[10], Joris Witstok[11,3], Benjamin D. Johnson[5], Stacey Alberts[10], Andrew J. Bunker[12], Stéphane Charlot[13], Daniel J. Eisenstein[5], Jakob M. Helton[10], Peter Jakobsen[11,14], Nimisha Kumari[15], Brant Robertson[16], Aayush Saxena[12,8], Hannah Übler[2,3], Christina C. Williams[17], Christopher N. A. Willmer[10], and Chris Willott[18]

[1] Scuola Normale Superiore, Piazza dei Cavalieri 7, I-56126 Pisa, Italy
[2] Kavli Institute for Cosmology, University of Cambridge, Madingley Road, Cambridge, CB3 0HA, UK
[3] Cavendish Laboratory, University of Cambridge, 19 JJ Thomson Avenue, Cambridge, CB3 0HE, UK
[4] INAF – Osservatorio Astronomico di Brera, via Brera 28, I-20121 Milano, Italy
[5] Center for Astrophysics | Harvard & Smithsonian, 60 Garden St., Cambridge MA 02138 USA
[6] Department of Space, Earth, & Environment, Chalmers University of Technology, Chalmersplatsen 4 412 96 Gothenburg, Sweden
[7] European Southern Observatory, Karl-Schwarzschild-Strasse 2, 85748 Garching, Germany
[8] Department of Physics and Astronomy, University College London, Gower Street, London WC1E 6BT, UK
[9] National Astronomical Observatory of Japan, 2 Chome-21-1, Osawa, Mitaka, Tokyo 181-8588, Japan
[10] Steward Observatory, University of Arizona, 933 N. Cherry Avenue, Tucson, AZ 85721, USA
[11] Cosmic Dawn Center (DAWN), Copenhagen, Denmark
[12] Department of Physics, University of Oxford, Denys Wilkinson Building, Keble Road, Oxford OX1 3RH, UK
[13] Sorbonne Université, CNRS, UMR 7095, Institut d'Astrophysique de Paris, 98 bis bd Arago, 75014 Paris, France
[14] Niels Bohr Institute, University of Copenhagen, Jagtvej 128, DK-2200, Copenhagen, Denmark
[15] AURA for European Space Agency, Space Telescope Science Institute, 3700 San Martin Drive, Baltimore, MD 21210, USA
[16] Department of Astronomy and Astrophysics University of California, Santa Cruz, 1156 High Street, Santa Cruz CA 96054, USA
[17] NSF's National Optical-Infrared Astronomy Research Laboratory, 950 North Cherry Avenue, Tucson, AZ 85719, USA
[18] NRC Herzberg, 5071 West Saanich Rd, Victoria, BC V9E 2E7, Canada

Received 1 October 2024 / Accepted 28 February 2025

ABSTRACT

JADES-GS-z14-0 is the most distant spectroscopically confirmed galaxy yet, at $z \gtrsim 14$. With a UV magnitude of –20.81, it is one of the most luminous galaxies at cosmic dawn and its half-light radius of 260 pc means that stars dominate the observed UV emission. We report the Atacama Large Millimeter/submillimeter Array (ALMA) detection of [O III]88 μm line emission with a significance of 6.67σ and at a frequency of 223.524 GHz, corresponding to a redshift of 14.1796 ± 0.0007, which is consistent with the candidate C III] line detected in the NIRSpec spectrum. At this spectroscopic redshift, the Lyman-α break identified with NIRSpec requires a damped Lyman-α absorber with a column density of $\log(N_{\rm HI}/{\rm cm}^{-2}) = 21.96$. The total [O III]88 μm luminosity ($\log(L_{\rm [OIII]}/{\rm L}_\odot) = 8.3 \pm 0.1$) is fully consistent with the local $L_{\rm [OIII]} - SFR$ relation and indicating a gas-phase metallicity >0.1 $Z_\odot$. Using `prospector` spectral energy distribution (SED) modeling and combining the ALMA data with JWST observations, we find $Z = 0.17\ Z_\odot$ and a non-zero escape fraction of ionizing photons (~11%), which is necessary by the code to reproduce the UV spectrum. We measure an [OIII]5007 Å/[OIII]88 μm line flux ratio between 1 and 20, resulting in an upper limit to the electron density of roughly 700 cm^{-3} assuming a single-cloud photoionization model. The [O III]emission line is spectrally resolved, with a FWHM of 102^{+29}_{-22} km s^{-1}, resulting in a dynamical mass of $\log(M_{\rm dyn}/M_\odot) = 9.0 \pm 0.2$. When compared to the stellar mass, this value represents a conservative upper limit on the gas mass fraction, which ranges from 50% to 80%, depending on the assumed star formation history. Past radiation-driven outflows may have cleared the galaxy from the gas, reducing the gas fraction and thus increasing the escape fraction of ionizing photons.

Key words. galaxies: evolution – galaxies: formation – galaxies: high-redshift – galaxies: ISM

1. Introduction

One of the most exciting and puzzling results to come out of observations with JWST is the discovery of numerous luminous ($M_{\rm UV} < -20$) galaxies already in place 300–500 Myr after the Big Bang (Arrabal Haro et al. 2023; Bunker et al. 2023; Curtis-Lake et al. 2023; Robertson et al. 2023; Wang et al. 2023; Castellano et al. 2024; Carniani et al. 2024; Zavala et al. 2024). Indeed, the number of such bright galaxies at $z > 10$ is up to one order of magnitude higher than what was extrapolated based on both pre-JWST observations and cosmological simulations (e.g., Finkelstein et al. 2023, Donnan et al. 2024, Robertson et al. 2024). Such observations have raised several questions about the formation of first galaxy populations, and

some studies have suggested a slow decline in the number density of galaxies at $z > 12$, with increasing efficiency of galaxy formation in halos at higher redshifts (e.g., Dekel et al. 2023; Robertson et al. 2024). Other studies suggest that the overabundance of UV-luminous galaxies can be also explained with an attenuation-free model (Ferrara et al. 2023; Ferrara 2024). This assumes that the radiation pressure of the stars expels gas and dust from the galaxy reducing the dust attenuation and boosting the observed UV emission. Alternatively, stochasticity in the galaxy luminosities and star-formation rate (SFR) at fixed halo mass (Mason et al. 2023; Mirocha & Furlanetto 2023; Shen et al. 2023), a top-heavy initial mass function (Inayoshi et al. 2022; Trinca et al. 2024), and a contribution from accreting black holes (Inayoshi et al. 2022; Trinca et al. 2024; Hegde et al. 2024) are other possible scenarios that can explain the observed UV luminosity function at the Cosmic Dawn.

The study of the UV luminosity function alone is not sufficient to distinguish the various models. However, each model is expected to make different predictions regarding the stellar population and interstellar medium (ISM) properties of such luminous galaxies; constraining these galaxies through observations would thus allow us to discern among the models and break the degeneracies encountered on the population level. However, the properties derived from the spectral energy distribution (SED) fitting of the most distant galaxies are not well-constrained and are highly degenerate between each other, particularly because the available photometry usually only probes the rest-frame UV emission (i.e., there is a strong degeneracy between the stellar mass, dust attenuation law, and star-formation history). To make further progress additional data at other wavelengths are extremely valuable.

To date, JADES-GS-z14-0 is the most distant galaxy known so far (Robertson et al. 2024; Helton et al. 2024; Carniani et al. 2024). With a UV luminosity of $M_{\rm UV} \sim -21$, this galaxy is among the most luminous galaxies at $z > 8$ in GOODS-S and GOODS-N CANDELS fields (Hainline et al. 2024a). It is two times more luminous than the GHZ2 at $z = 12.33$ ($M_{\rm UV} \sim -20.5$; Castellano et al. 2024) and nearly as luminous as GN-z11 at $z = 10.6$ ($M_{\rm UV} \sim -21.5$; Tacchella et al. 2023; Bunker et al. 2023). NIRCam observations reveal that JADES-GS-z14-0 is spatially resolved with a half-light radius of 260 pc (0.079″), indicating its emission is dominated by light from the stellar population and does not arise from an active galactic nucleus (AGN). The galaxy has also been detected in a 43-h MIRI pointing at 7.7 μm, with excess wide-band emission likely indicating strong emission lines from [O III]$\lambda\lambda$4959, 5007 and Hβ, corresponding to a rest-frame equivalent width EW([O III]$\lambda\lambda$4959, 5007 + Hβ) = 370 Å (Helton et al. 2024).

The JWST/NIRSpec follow-up observations have revealed a prominent sharp Lyman-α break, indicating a redshift of $z = 14.32^{+0.08}_{-0.20}$ (Carniani et al. 2024). As the Lyman-α break profile is sensitive to the column density of neutral hydrogen along the line of sight, the uncertainties on the spectroscopic redshift are quite large and asymmetric toward low values, whose probability is not negligible given the recent discovery of damped Lyman systems at very high redshifts (Hsiao et al. 2024a; Heintz et al. 2025; D'Eugenio et al. 2024a; Hainline et al. 2024b; Witstok et al. 2024). Despite the deep observations, the NIRSpec spectrum does not show any clear rest-frame UV emission lines. There is only a tentative (3.6σ) detection of C III] $\lambda\lambda$1907, 1909 at 2.89 μm, which would yield a redshift of 14.178 ± 0.013. If this redshift is confirmed, it would require the presence of a damped Lyman-α absorber (DLA) with a hydrogen column density of $\log(N_{\rm HI}/{\rm cm}^{-2}) = 22.23$ to explain the redshifted Lyman-α break (Carniani et al. 2024).

The SED fitting of JWST photometric and spectroscopic data indicates an ongoing star-formation rate (SFR) of 19 $M_\odot$/yr and a stellar mass of 4×10^8 $M_\odot$. The latter suffers from large uncertainties (0.4 dex) due to the unknown origin of the excess MIRI flux at 7 μm (Helton et al. 2024). The spectral modeling suggests that one-third of the MIRI flux is associated with the rest-optical nebular emission lines [O III]$\lambda\lambda$4959, 5007 and Hβ, but the results depend on the star-formation history priors adopted in the SED fitting (Which are highly uncertain at these high redshifts, Tacchella et al. 2022a; Whitler et al. 2023).

The absence of bright UV emission lines in NIRSpec spectrum sets only upper limits (with significant uncertainties) on the properties of the ISM. Additional multi-wavelength observations are thus fundamental to constrain the galaxy and ISM properties and provide deeper insights into the galaxy evolution of JADES-GS-z14-0.

In this paper, we combine JWST data with the public ALMA observations (DDT 2023.A.00037.S, PI: S. Schouws) of JADES-GS-z14-0. The observations carried out in the frequency range between 218 and 229 GHz allow us to identify the far-infrared oxygen line [O III]at rest-frame 88 μm and determine the redshift of the galaxy with high accuracy. In addition to that, the far-infrared line probes the gas-phase metallicity and then, combined with the MIRI data, allows us to constrain the electron density. Finally, the continuum emission allows us to study the dust content and investigate the nature of the moderate optical dust attenuation ($A_{\rm V} = 0.3$) determined from the JWST data.

Throughout this paper, we adopt the standard cosmological parameters $H_0 = 70$ kms^{-1} Mpc^{-1}, $\Omega_{\rm M} = 0.30$, $\Omega_\Lambda = 0.70$, according to which 1 arcsec at $z = 14$ corresponds to a proper distance of 3.268 kpc. Astronomical coordinates and magnitudes are given in the ICRS and AB systems, respectively. Abundance patterns are from Byler et al. (2017) unless otherwise stated.

2. ALMA observations and data reduction

JADES-GS-z14-0 was observed with ALMA Band 6 as part of 2023.A.00037.S program, in two spectral configurations to target the [O III] 88 μm emission line and cover 98% of the redshift probability distribution reported in Carniani et al. (2024). Each spectral configuration was observed for 2.82 hours of on-source integration time. The calibrated visibilities were downloaded from the ALMA archive. The first spectral configuration was observed with ALMA configuration C4, while the second one with configuration C5, hence the two spectral configurations have different spatial resolutions.

We performed the cleaning on the calibrated visibilities using the Common Astronomy Software Applications package (CASA; McMullin et al. 2007) task `tclean`. To optimize the sensitivity to detect the [O III] emission line, we adopted a natural and briggs robust=0.5 weighting scales, hogbom deconvolver, a spaxel scale of 0.1″, and a channel width of 10 km s^{-1} to create the final datacubes. The final datacubes for the first spectral configuration have a beam size of 0.82″ × 0.60″ and 1.09″ × 0.82″ for the briggs robust=0.5 and natural cubes, respectively. For the second spectrum configuration, we obtain datacubes with 0.42″× 0.38″ and 0.58 ″× 0.50 ″ for the briggs robust=0.5 and natural cubes, respectively.

We also imaged the dust-continuum emission at 88 μm rest-frame by using the "mfs" mode of the task tclean using natural weighting to maximize the signal-to-noise ratio (S/N). The final

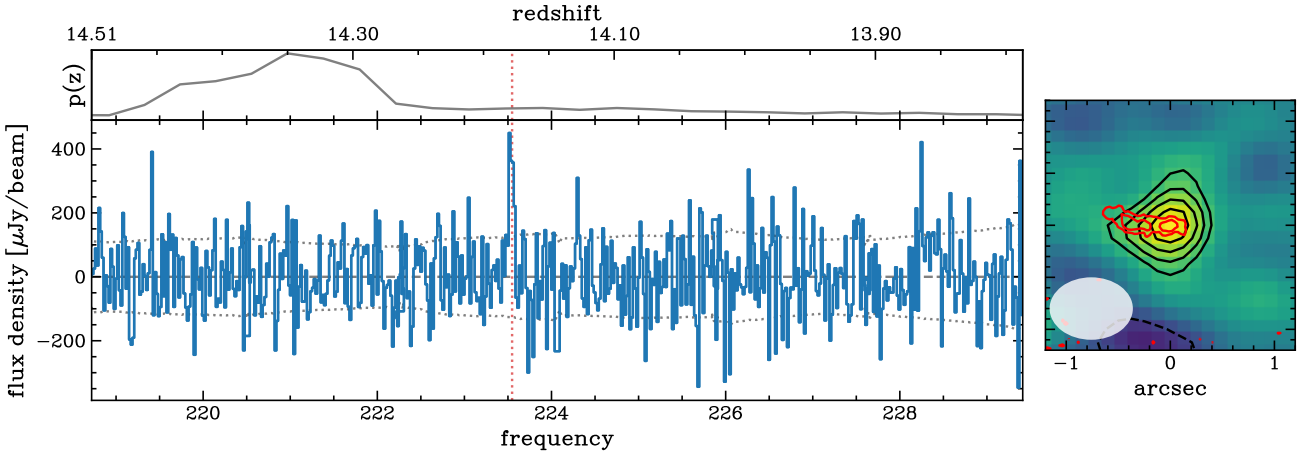

Fig. 1. [O III]88 μm spectrum (left) and flux map (right) of JADES-GS-z14-0. The top panel illustrates the redshift probability distribution determined from the JWST/NIRSpec data. The red vertical dotted line shows the redshift determined from the candidate C III] detection (Carniani et al. 2024). The black contours in the flux map show ±3, ±4, ±5, and ±6 σ of [O III]emission, while red contours correspond to the rest-frame UV emission from JWST/NIRCam F200W observations.

continuum image has a beam size of 0.66″ × 0.84″ and a sensitivity of 4.4 μJy beam^{-1}.

3. Data analysis

The frequency range of these ALMA observations covers about 98% (Fig. 1) of the posterior distribution function of the spectroscopic redshift determined from the fitting of the Lyman-break profile of JWST/NIRSpec data (Carniani et al. 2024). Given the large uncertainty on the spectroscopic redshift, we have performed a blind-line search in the ALMA datacube. In particular, we have analyzed the region of the datacube enclosed within 5 arcsec from the location of the target. The adopted customized line finder code was already used in other ALMA studies (e.g., Maiolino et al. 2015; Carniani et al. 2017, 2020) and was optimized to identify point-like sources in datacubes without defining a priori the line width of the emission line. More details of the code are explained in Appendix B of Carniani et al. (2020).

At the location of the galaxy, we have identified an [O III] emission line with a significance level at 6.67σ at a frequency of 223.524 GHz, which corresponds to a redshift of 14.1796 ± 0.0007. Fig. 1 shows the spectrum of the detected line and the integrated map. The line has a full width at half maximum (FWHM) of 102^{+29}_{-22} km s^{-1} and an integrated flux density of 0.037 ± 0.009 Jy km s^{-1}, resulting in an [O III] luminosity $\log(L_{[OIII]}/L_{\odot}) = 8.3 \pm 0.1$. We checked whether the detection could be due to a line associated to the foreground galaxy at $z = 3.475$ located close to JADES-GS-z14-0 to its East (Carniani et al. 2024). We find no line species that would be redshifted to a frequency of 223.524 GHz given the above redshift.

We have also analyzed the continuum map, but no signal at the spatial position of the [O III]88 μm line emission has been detected. We have thus derived a 3σ upper limit on the continuum emission for a point-like source of $S_{88\,\mu m} < 13$ μJy.

The fidelity of the ALMA emission line detection is verified in Appendix A. We note that there is an additional 3.7σ signal in the [O III]moment-0 map at the same redshift 2.5 arcsec NW from JADES-GS-z14-0. Given the low significance and the lack of continuum detection in the NIRCam images, we do not consider this additional 3.7-σ signal as a solid detection.

4. Results

4.1. Dust content

As the dust thermal emission is not detected in the ALMA continuum map at 88 μm, we estimate an upper limit on dust mass. We assume a typical single-temperature modified black body function (e.g., Eq. (1) in Carniani et al. 2019) to reproduce the dust thermal emission spectral-energy distribution in the rest-frame far-infrared. We adopt a dust opacity coefficient at 250 GHz of 0.45 g cm^{-2} and an emissivity index of $\beta = 1.8$ (Witstok et al. 2023), and correct for the effect of the cosmic microwave background following da Cunha et al. (2013). Given the modified black body function, the flux at 88 μm depends on dust mass and temperature.

Figure 2 shows the 3σ upper limits on the dust mass as a function of the dust temperature, based on the continuum sensitivity of the DDT ALMA program. The dust mass cannot be constrained with only one ALMA measurement due to the degeneracy with the dust temperature. In addition to that, if we assume that the dust temperature is lower than 60 K, the continuum sensitivity is not sufficient to put any constraint on the dust enrichment mechanism. The upper limits on the dust-to-stellar mass ratio at low temperatures are higher than 0.002 (vertical black dashed line in Figure 2). Such value is higher than the typical dust-to-stellar mass ratio observed in high-z galaxies (Witstok et al. 2022) and expected by theoretical models assuming that at such early times dust enrichment mechanism is mainly associated with supernova ejecta (Schneider & Maiolino 2024). This means that in the hypothesis of low temperatures, the depth of current observations is not sufficient to put any constraints on the dust content.

We note that the upper limit on the continuum emission is consistent with the recent predictions by Ferrara et al. (2025). The authors show that the flux at 88 μm depends on both the dust-to-stellar mass ratio and the extension of the dust. In their fiducial case with dust-to-stellar equal to 1/529, the dust is expected to be extended up to 1.4 kpc to reproduce the inferred A_V from Carniani et al. (2024), have a luminosity-weighted temperature of 72 K, and a flux of about 15 μJy. In conclusion, the continuum sensitivity of this DDT program does not provide any information about the dust content in JADES-GS-z14-0 and deeper future observations are needed to unveil the dust content

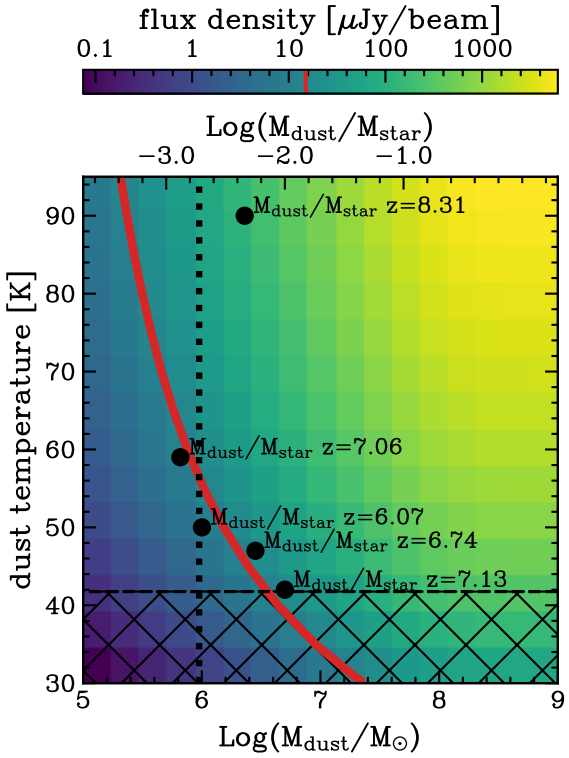

Fig. 2. Predicted continuum flux density at the rest-frame wavelength 88 μm as a function of dust temperature and dust mass. The red line shows the 3σ sensitivity of the DDT ALMA program of JADES-GS-z14-0. The top axis shows the dust-to-stellar mass ratio for the stellar mass of JADES-GS-z14-0 ($M_{\rm star}$ = $10^{8.6}$ $M_\odot$). The vertical dashed line shows the expected dust-to-stellar mass ratio for the supernova dust enrichment mechanism, and black circles illustrate the current measurements in galaxies at $z > 7$. The CMB temperature at $z = 14$ is 41.7 K (dashed region).

in the galaxy and investigate the formation (and destruction) of dust grains in the early Universe.

4.2. DLA

We detect an emission line at 6.7σ which we associate with the [O III] 88 μm transition, implying a spectroscopic redshift of $z = 14.1796 \pm 0.0007$. The [O III]redshift is within the probability distribution function of redshifts inferred from the Lyman break analysis for this galaxy (top panel of Figure 1) and is consistent with the redshift from the tentative detection of C III] of 14.178 ± 0.013 (Carniani et al. 2024). This redshift, however, is lower than what was predicted from the Lyα break alone ($z = 14.32$), and indicates the presence of additional damped Lyα absorption for the source, in agreement for what has been observed in other galaxies at $z > 10$ (Heintz et al. 2024; Umeda et al. 2024; D'Eugenio et al. 2024b; Hainline et al. 2024b; Heintz et al. 2025; Witstok et al. 2024).

Using the redshift determined from the detected far-infrared line, we explore the potential need for a DLA to explain the Lyman break profile. To that end, we fit the slit-loss-corrected NIRSpec spectrum with a power-law function of the form $f_\lambda \propto \lambda^{-\beta}$ and apply the attenuation we would expect from the host galaxy ISM or circumgalactic medium column density of neutral hydrogen ($N_{\rm HI}$) along the line of sight as modeled in Witstok et al. (2024) and Hainline et al. (2024b). From this fit, we measure a hydrogen column density of $\log(N_{\rm HI}/{\rm cm}^{-2}) = 22.23$ for JADES-GS-z14-0.

This column density, which is similar to those measured in other, intrinsically fainter, high-redshift galaxies, indicates the presence of a large reservoir of pristine gas surrounding JADES-GS-z14-0. The presence of a strong DLA in JADES-GS-z14-0 may indicate that we are observing the source still in the process of assembly and growth. This result may be surprising given its observed brightness and the lack of similar sources found at later cosmic times (Carniani et al. 2024). The location, and extent of the DLA with respect to the host galaxy is still uncertain, however.

The smoothness of the Lyα break, implied by the redshift measured via [O III]and C III] being slightly lower than expected from the break alone, can alternatively be explained by invoking an unusually strong two-photon nebular continuum (Katz et al. 2024). This would require the nebular continuum to dominate in the rest-frame UV, which only occurs in the presence of very hot ionizing sources ($T_{\rm eff} \gtrsim 10^5$ K) and at gas densities of $n \lesssim 10^5$ cm^{-3} (Cameron et al. 2024). In this case, the two-photon radiative decay from the 2s state produces prominent continuum emission with a characteristic, fixed shape featuring a smooth 'rollover' redwards of Lyα similar to DLA absorption (Spitzer & Greenstein 1951).

4.3. [OIII] 88 μm luminosity

We inferred the [O III]88 μm luminosity from the 6.7σ detection at 223.524 GHz. We estimated the measured [O III] luminosity by following Carilli & Walter (2013) and corrected for a modest lensing magnification factor of 1.17 (Carniani et al. 2024), resulting in $\log_{10}(L_{\rm [OIII]}/L_\odot) = 8.3 \pm 0.1$. We compare the [O III] luminosity to the SFR in the top panel of Figure 3, alongside other high-redshift detections (Harikane et al. 2020; Witstok et al. 2022; Fujimoto et al. 2024) and local low-metallicity dwarf galaxies (De Looze et al. 2014).

The [O III]detection of JADES-GS-z14-0 falls slightly below the local and high-z [O III]-SFR observed relations but they agree within the uncertainties. This excludes that JADES-GS-z14-0 is extremely metal-poor ($Z < 0.05\ Z_\odot$). Indeed, as shown in the bottom panel of Figure 3, the [O III]depends both on SFR and gas-phase metallicity, and galaxies with $Z < 0.05\ Z_\odot$ fall below the local relation. For example, IZw18 and SBS0335-052, which have a gas-phase metallicity of about 3% solar (De Looze et al. 2014), show a $L_{\rm [OIII]}$ deficit of 0.2–0.3 dex relative to the local relation. The ratio between $L_{\rm [OIII]}$ and SFR of JADES-GS-z14-0 is similar to those measured in dwarf galaxies with $0.05\ Z_\odot < Z < 1\ Z_\odot$. However, we cannot exclude a lower metallicity scenario given that $L_{\rm [OIII]}$/SFR is also sensitive to the ionization parameter and electron density.

In Figure 4 we combine JWST/MIRI and ALMA data to determine the region covered by JADES-GS-z14-0 in the $L_{\rm [OIII]5007\,Å}/L_{\rm H\beta}$ versus $L_{\rm [OIII]5007\,Å}/L_{\rm [OIII]88\,\mu m}$ diagram. Since [O III]λ5007 and Hβ are not spectrally resolved in MIRI, we vary $L_{\rm [OIII]5007\,Å}/L_{\rm H\beta}$ from 0.1 to 10, which is a plausible range for metal-poor galaxies with different ionization conditions. For each combination of $L_{\rm [OIII]5007Å}/L_{\rm H\beta}$, we use the MIRI excess flux at 7 μm ($\Delta f = 27.5 \pm 5.6$ nJy; Helton et al. 2024) as the total flux of the blend, and calculate the possible value of $L_{\rm [OIII]5007\,Å}$ and thus $L_{\rm [OIII]5007\,Å}/L_{\rm [OIII]88\,\mu m}$. The dark magenta-shaded region reported in Figure 4 shows the range of line ratios assuming that the stellar age of the galaxy is 50−100 Myr and thus the stellar continuum emission at 7.7 μm is as strong as that at 4.4 μm (see details in Appendix B). The light

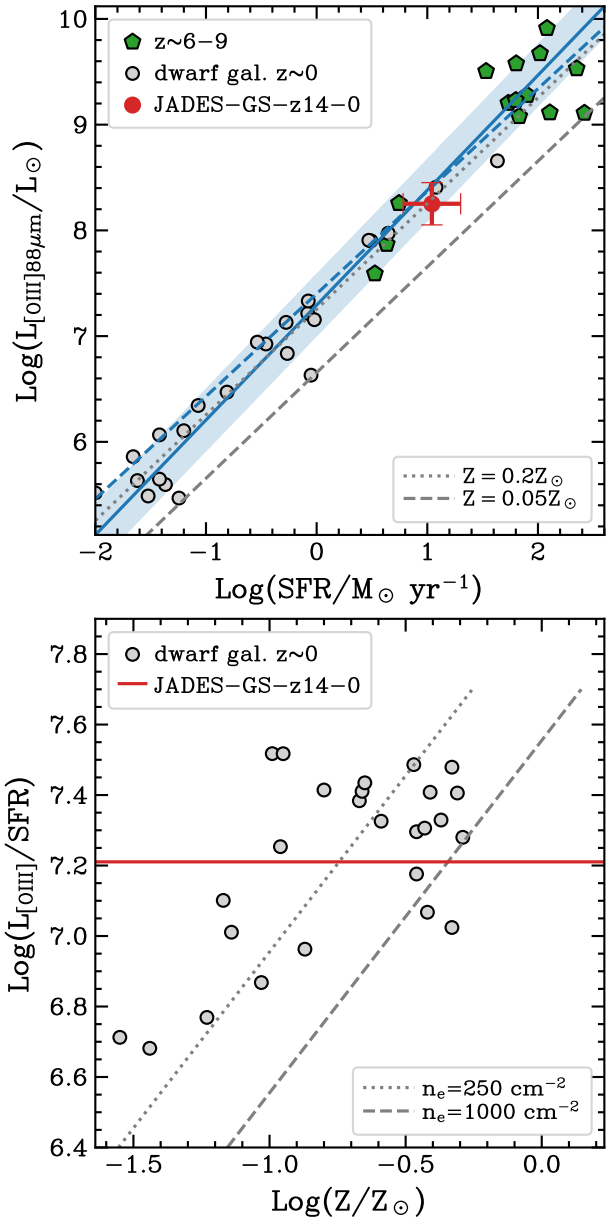

Fig. 3. $L_{[\mathrm{OIII}]}$ versus SFR (top panel) and $L_{[\mathrm{OIII}]}$/SFR versus gas-phase metallicity (bottom panel). The red circle and horizontal line (in top and bottom panels, respectively) mark the measurement for JADES-GS-z14-0. Gray circles are local dwarf galaxies, while green pentagons are $z \sim 6-9$ galaxies. The solid blue line shows the local relation by De Looze et al. (2014) for metal-poor galaxies, with the shaded area corresponding to the 1σ uncertainty. The blue dashed line illustrates the $L_{[\mathrm{OIII}]}$ − SFR relation for high-z galaxies by Harikane et al. (2020). Dotted and dashed gray lines illustrate the Cloudy models for different gas-phase metallicities and electron densities (Harikane et al. 2020; Jones et al. 2020).

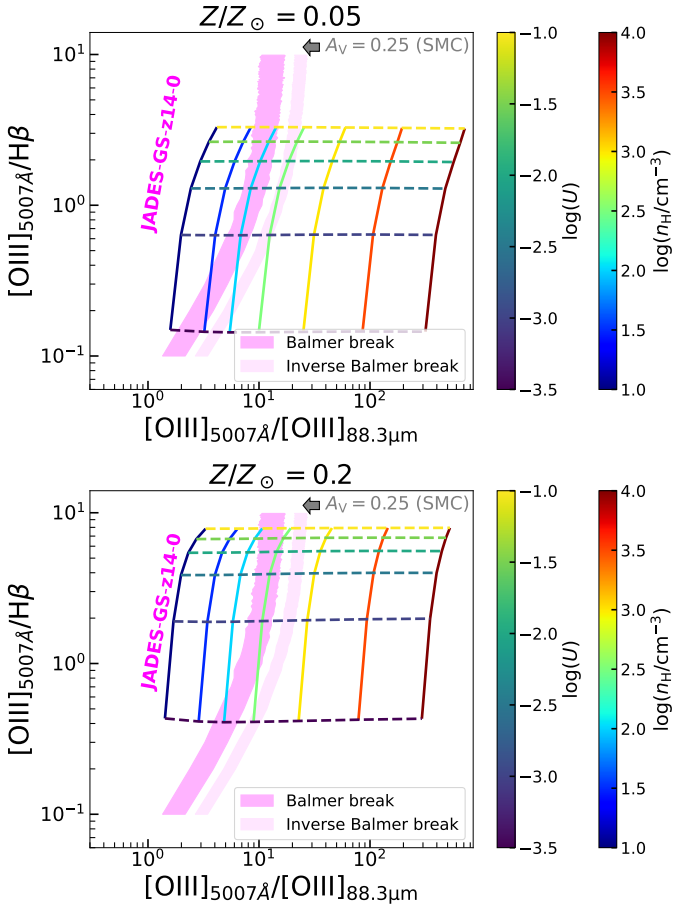

Fig. 4. [O III]5007 Å/[O III]88 μm versus [O III]5007Å/Hβ diagram. Top and bottom panels show model grids computed with CLOUDY with metallicities $Z/Z_{\odot} = 0.05$ to $Z/Z_{\odot} = 0.2$, respectively. Each model grid spans a range of ionization parameters ($-3.5 \leq \log U \leq -1$) and hydrogen densities ($10\ \mathrm{cm}^{-3} \leq n_{\mathrm{H}} \leq 10^{4}\ \mathrm{cm}^{-3}$) in steps of 0.5 dex. Details on model parameters are provided in Table 1. The magenta-shaded regions show the plausible attenuation-corrected line ratios for JADES-GS-z14-0 inferred from observations by JWST/MIRI and ALMA. The dark regions report the range of line ratios assuming that the MIRI excess is only due to the optical line. The light regions illustrate the range of line ratios in the case the stellar age is 1 Myr and there is an inverse Balmer break in the spectrum. The gray arrow represents a reddening vector with $A_{\mathrm{V}} = 0.25$ assuming the nebular dust attenuation follows an average SMC extinction curve.

magenta-shaded regions illustrate the extreme case in which there is an inverse Balmer break in the spectral due to a young (<5 Myr) stellar population in the galaxy (Appendix B). We stress that the $L_{[\mathrm{OIII}]5007\,\text{Å}}$ and $L_{\mathrm{H}\beta}$ inferred directly from the SED fitting cannot be used in this analysis because the fitting process and thus the intensity of the emission lines are inferred assuming a fixed electronic density.

The line ratios we show are corrected for dust attenuation. To illustrate the effect of dust attenuation, we plot a reddening vector corresponding to $A_{\mathrm{V}} = 0.25$ (as extreme value determined by the SED fitting later in Sect. 5) assuming an average SMC extinction law (Gordon et al. 2003). Due to the low A_{V}, the reddening correction for $L_{[\mathrm{OIII}]5007\,\text{Å}}/L_{[\mathrm{OIII}]88\,\mu\mathrm{m}}$ is not sensitive to the choice of the extinction curve.

For comparison, we also show in Figure 4 predictions from photoionization single-density component models computed with the code CLOUDY (c17.03, Ferland et al. 2017) with a range of metallicities, ionization parameters, and gas densities. We summarize the full set of model parameters in Table 1. In brief, we assume the gas is photoionized by radiation from a 1 Myr-old simple stellar population (SSP) generated by the Binary Population and Spectral Synthesis code (BPASS v2.3, Eldridge et al. 2017; Stanway & Eldridge 2018; Byrne et al. 2022). We allow the stellar metallicity to vary from 5% solar to 20% solar and match the gas-phase metallicity with the stellar metallicity. Dust depletion is included such that 40% of oxygen from the gas

Table 1. Input parameters for CLOUDY photoionization models.

Parameter	Values
$Z/Z_\odot$	0.05, 0.1, 0.2
$\log U$	−3.5, −3, −2.5, −2, −1.5, −1
$\log(n_H/\mathrm{cm}^{-3})$	1, 1.5, 2, 2.5, 3, 3.5, 4
EoS	Constant gas pressure
SED	1 Myr SSP from BPASS
Solar abundance set	Grevesse et al. (2010) abundance set
N/O (C/O) vs. O/H	Groves et al. (2004) relation
He/H vs. O/H	Dopita et al. (2000) relation
Dust depletion	Cowie & Songaila (1986); Jenkins (1987) depletion factors
Atomic data	CHIANTI (v7; Dere et al. 1997, Landi et al. 2013)

is depleted onto dust grains (Cowie & Songaila 1986; Jenkins 1987). We vary the dimensionless ionization parameter, defined as $U \equiv Q_0/n_H c$ (Q_0 is the ionizing photon flux, n_H is the hydrogen density, and c is the speed of light), from −3.5 to −1, and the density in a range of $10 \leq n_H/\mathrm{cm}^{-3} \leq 10^4$. For the equation of state (EoS), we assume the gas is isobaric.

The constraints imposed by the ALMA and MIRI observations set upper limits on the electron density (n_e) of [O III]88 µm-emitting regions of JADES-GS-z14-0 depending on the metallicity. By interpolating the model grids linearly in the logarithmic space of n_H and U using the GRIDDATA function in the SCIPY package (Virtanen et al. 2020), we obtain density upper limits of $n_{H;uplim} = 180\ \mathrm{cm}^{-3}$ ($Z/Z_\odot = 0.05$), $300\ \mathrm{cm}^{-3}$ ($Z/Z_\odot = 0.1$), and $420\ \mathrm{cm}^{-3}$ ($Z/Z_\odot = 0.2$) after dust attenuation corrections. In the inverse Balmer break scenario, which corresponds to a stellar age of less than 5 Myr, we determine an upper limit for the electronic density of $n_H^{uplim} = 700\,\mathrm{cm}^{-3}$ at $Z/Z_\odot = 0.2$. We emphasize that this upper limit is highly conservative, even when considering the possibility of multiple-density regions within the galaxy. Specifically, if a fraction of the [O III] 5007 emission arises from regions with electronic densities exceeding the critical density of [O III] 88 µm (~500–1000 cm^{-3}), where [O III] 88 µm is not emitted, the $L_{[\mathrm{O\,III}]\,5007\,\text{Å}}/L_{[\mathrm{O\,III}]\,88\,\mu\mathrm{m}}$ ratio and consequently the inferred electronic density would be lower than the value reported in Figure 4. In summary, we conclude that the [O III] 88 µm-emitting regions in JADES-GS-z14-0 have an electronic density below 700 cm^{-3}. However, JADES-GS-z14-0 may also contain denser star-forming regions that are not effectively probed by [O III] 88 µm. High-spectral-resolution observations of C III] doublet could provide a valuable diagnostic for the electronic densities in these regions (James et al. 2014; Mingozzi et al. 2022).

The upper limits on the densities determined from the optical [O II]$\lambda\lambda$3726,3729 doublet, which has a critical density comparable to that of [O III]88µm, are comparable to those found in galaxies at $z = 2-3$ (e.g., Sanders et al. 2016; Kashino et al. 2017; Strom et al. 2017; Davies et al. 2021), but appear lower than galaxies at $z > 8$ (e.g., Isobe et al. 2023; Abdurro'uf et al. 2024; Marconcini et al. 2024). For example, Isobe et al. (2023) find that galaxies at $z = 4-9$ have electron densities higher than $n_e \sim 300\ \mathrm{cm}^{-3}$ ($n_e \approx 1.1\ n_H$ for H II regions), and the median value for $z = 7-9$ is $n_e \sim 1000\ \mathrm{cm}^{-3}$. Furthermore, n_e might further increase with increasing z if the relation given by Isobe et al. (2023) is extrapolated to $z > 9$. As another example, based on the ALMA observation of GHZ2, a bright galaxy at $z = 12.33$, Zavala et al. (2024) infer a density of $n_e = 100 - 3000\ \mathrm{cm}^{-3}$ or higher depending on the assumed temperature. However, we caution that the above high-redshift results are currently based on small number statistics and might be subject to measurement systematics (Sanders et al. 2024).

From Figure 4, one can see a degeneracy between the ionization parameter and the metallicity. If we constrain $n_e \gtrsim 300\ \mathrm{cm}^{-3}$ (i.e., to be higher than the average density in SF galaxies at $z = 2-3$, Sanders et al. 2016; Strom et al. 2017), then only the highest metallicity model with $Z/Z_\odot = 0.2$ [$(\mathrm{O/H})_{gas}/(\mathrm{O/H})_{solar} = 0.12$ after dust depletion] is able to reproduce the observed line ratios, which also constrain the ionization parameter to be $-3 \lesssim \log U \lesssim -1.5$. Considering an observed scatter of roughly $100\ \mathrm{cm}^{-3}$ in the density (Sanders et al. 2016; Strom et al. 2017), models with $Z/Z_\odot = 0.1$ [$(\mathrm{O/H})_{gas}/(\mathrm{O/H})_{solar} = 0.06$] and $-3 \lesssim \log U \lesssim -1.5$ are also plausible. Again, we caution that the current constraint on the densities at high redshift has large uncertainties and we cannot exclude the possibility that JADES-GS-z14-0 is a low-density outlier at high redshift.

5. SED modeling: NIRSpec+NIRCam+MIRI+ALMA

5.1. Stellar mass

The combination of ALMA and JWST provides us with new constraints on the SED modeling. We add our ALMA constraints to existing NIR and MIR data; we use NIRSpec/MSA spectroscopy and NIRCam photometry from Carniani et al. (2024), in combination with MIRI F770W photometry from Helton et al. (2024, capturing Hβ and [O III]$\lambda\lambda$4959, 5007). We adopt the Bayesian inference framework `prospector` (Johnson et al. 2021), itself relying on `fsps` (Conroy et al. 2009; Conroy & Gunn 2010) for stellar spectra, and on pre-computed nebular emission from Byler et al. (2017). In our setup, we use MIST isochrones (Choi et al. 2016) and the C3K model atmospheres (Conroy et al. 2019). We use a recent implementation[1]. We generally follow the model setup of Tacchella et al. (2022b, hereafter T22). The differences are the IMF (we assume a Chabrier 2003 IMF with lower and upper mass limits of 0.1 and 300 $M_\odot$), a stronger prior on the parameters of the Kriek & Conroy (2013) dust attenuation, the inclusion of a 2nd-order multiplicative Chebyshev polynomial (to match the shapes of the photometry and of the spectrum), the maximum allowed redshift (no star formation is allowed earlier than $z = 30$), the addition of a DLA (with variable redshift and column density), and a rising prior on the star-formation history (SFH), following the redshift evolution of the accretion rate of dark-matter haloes. The rising prior is parameterized by the log-ratio of the SFR between each time bin and the previous bin in cosmic time; by default, this prior behaves similarly to the delayed-τ models, but we allow substantial freedom by using a probability prior on the log SFR ratio that is a Student's t distribution with scale 1 and $\nu = 2$ (following Leja et al. 2019). The rising prior on the SFH follows the mass accretion rate of dark-matter halos (Tacchella et al. 2018), and will be presented in Turner et al. (2025). The shape of this prior is shown in Fig. 5f (gray shaded region). The model attempts to reproduce the spectrum (modulo the polynomial scaling), the NIRCam–MIRI photometry, and the ALMA observations, both the [O III]λ88 µm line flux and the upper limit on the flux density of the dust continuum. The NIRSpec and NIRCam data are from Carniani et al. (2024), the MIRI data is from Helton et al. (2024). Given the redshift measurement from ALMA, we impose a strong Gaussian prior

[1] In particular, we employed development branch 'v2', build 1.2.1.dev103+gb055d6f.d20240919.

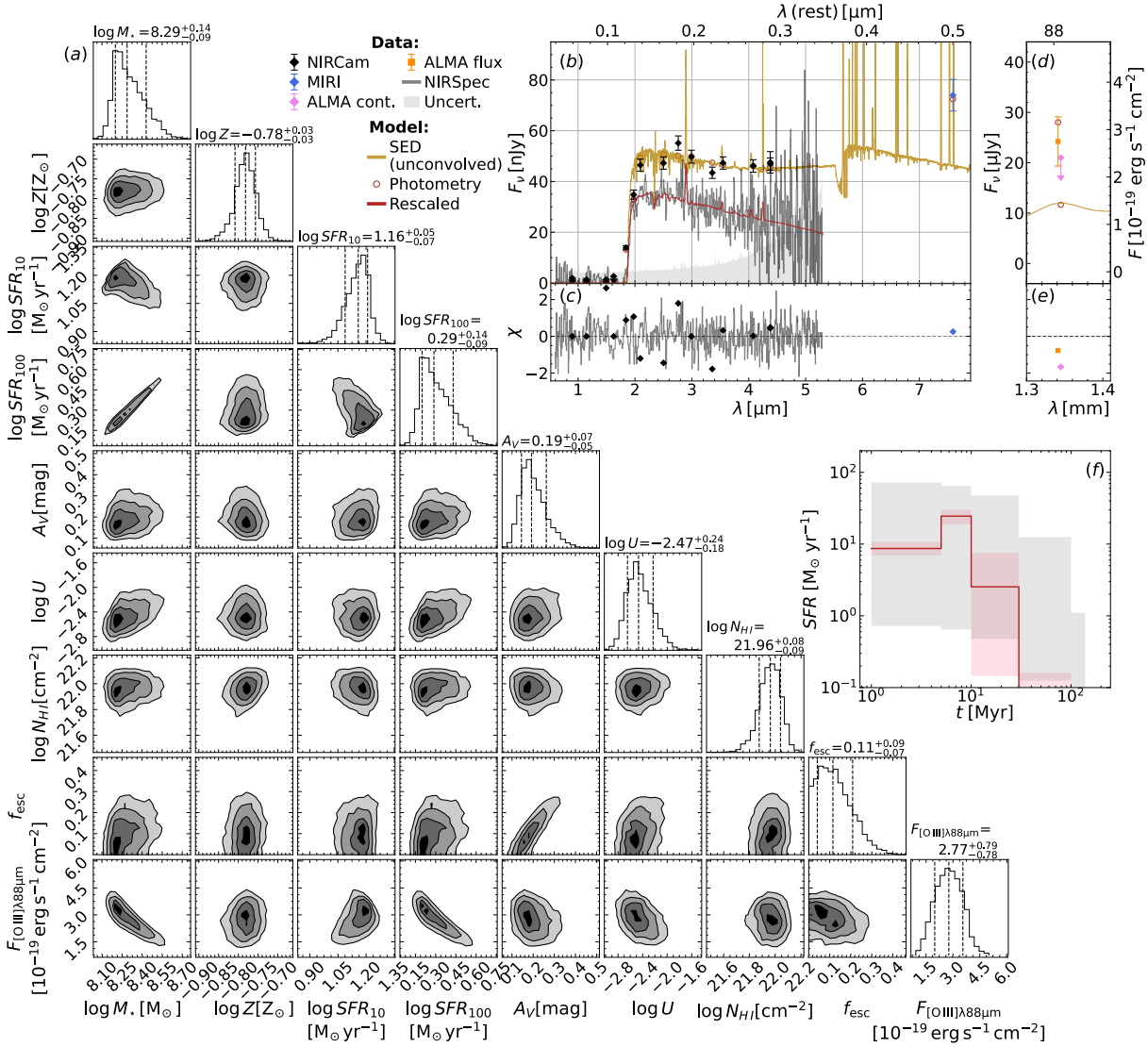

Fig. 5. Summary of `prospector` SED model. Panel a: Triangle diagram with the marginalized posterior distribution over a subset of the model-free or dependent parameters (see Table 2 for a description of the parameters and their probability prior). Panel b: SED, including wide- and medium-band measured flux densities (diamonds), the spectrum (grey line with grey region as the uncertainty). NIRCam, MIRI and ALMA data are in black, blue and pink, respectively. Model predictions are red circles (flux densities) or the red line (spectrum). The sand-coloured line is the model SED without convolving to the spectral resolution fo the data. Panel c: Model residuals normalised by the uncertainties. Panel d: Same as panel b, but for the FIR region. The orange square is the ALMA [O III]flux. Panel e: Same as panel c, but for the FIR region. Panel f: Star-formation history (red), with the prior probability in grey.

centered on $z = 14.1796$ with dispersion 0.0001. A summary of the model parameters is reported in Table 2. We infer the posterior probability distribution of our model parameters using `dynesty` (Speagle 2020; Koposov et al. 2022). The 1-d marginalized posteriors are also listed in Table 2. Fig. 5 reports the main 1-d and 2-d posterior probabilities (triangle diagram; Fig. 5a), the galaxy's SED (Fig. 5b), the normalized residuals (Fig. 5c), and the SFH (Fig. 5d). When fitting spectroscopy, the S/N of the data is much higher than for photometry, resulting in significantly smaller uncertainties. The result is that our posterior probabilities are dominated by systematic uncertainties. To estimate their magnitude, we run PROSPECTOR five times using the same data but different priors.

With this setup, we find fiducial (magnification-corrected) $\log M_\star/M_\odot = 8.29^{+0.14}_{-0.09}(^{+0.4}_{-0.1}$ systematics) and a $\log \mathrm{SFR}/(M_\odot\ \mathrm{yr}^{-1}) = 1.16^{+0.05}_{-0.07}(\pm 0.1)$. We report the star-formation rate averaged over the previous 10 Myr. To match the redshift of [O III]λ88 μm with that of the Lyα drop, the model also requires a DLA, with $\log N_{\rm HI}/\mathrm{cm}^{-2} = 21.96^{+0.08}_{-0.09}(\pm 0.01)$; this value is in agreement with the fiducial DLA model which gives a value of 22.23 (Section 4.2). We rule out a major role of wavelength-calibration issues between ALMA and NIRSpec, because the redshift from ALMA matches the 3-σ tentative detection of C III] from NIRSpec itself. The results are in agreement with the power-law fits reported in Section 4.2. We find a metallicity of 0.17 solar, somewhat higher than previous results (Carniani et al. 2024; Helton et al. 2024); this could be driven by the [O III] 88μm detection. Our setup finds a lower dust attenuation value and escape fraction than Carniani et al. (2024), however, these two parameters are unsurprisingly degenerate. In our fiducial model, the model preference for a low dust attenuation requires a strong nebular continuum to explain the relatively flat UV slope reported by Carniani et al. (2024); this is evident from the presence of a Balmer jump in

Table 2. Summary of the parameters, prior probabilities, and posterior probabilities of the fiducial `prospector` SED model (see also Fig. 5a).

	Parameter (1)	Free (2)	Description (3)	Prior (4)	Posterior (5)
Star-forming component	$z_{\rm obs}$	Y	Redshift	$\mathcal{N}(z_{\rm spec}, 0.001)$	$14.178^{+0.001}_{-0.001}$
	$\log M_\star[{\rm M}_\odot\,\mu^{-1}]$ (†)	Y	Total stellar mass formed	$\mathcal{U}(6, 10)$	$8.29^{+0.14}_{-0.09}$ ($^{+0.4}_{-0.1}$)
	$\log Z[{\rm Z}_\odot]$	Y	Stellar and gas metallicity	$\mathcal{U}(-2, 0)$	$-0.78^{+0.03}_{-0.03}$ (±0.03)
	log SFR ratios	Y	Ratio of the log SFR of non-parametric SFH	$\mathcal{T}(R(z)$ (‡), 1, 2)	–
	$\sigma_\star$ [km s^{-1}]	Y	Stellar intrinsic velocity dispersion	$\mathcal{U}(0, 300)$	190^{+70}_{-70}
	n	Y	Power-law modifier of the dust curve (T22, Eq. (5))	$\mathcal{G}(0, 0.1; -1.0, 0.2)$	$0.06^{+0.05}_{-0.04}$
	τ_V	Y	Optical depth of the diffuse dust (T22, Eq. (5))	$\mathcal{U}(0, 2)$	$0.19^{+0.07}_{-0.05}$
	$\mu_{\rm d}$	Y	Ratio of optical depths of the birth clouds and τ_V	$\mathcal{G}(1, 0.1; 0, 2)$	$0.94^{+0.06}_{-0.07}$
	$\sigma_{\rm gas}$ [km s^{-1}]	Y	Intrinsic velocity dispersion of the star-forming gas	$\mathcal{U}(0, 1500)$	$1,310^{+90}_{-100}$
	$\log U$	Y	Ionization parameter of the star-forming gas	$\mathcal{U}(-4, -1)$	$-2.47^{+0.24}_{-0.18}$
	$f_{\rm esc}$	Y	Birth-cloud escape fraction of ionizing radiation	$\mathcal{U}(0, 1)$	$0.11^{+0.09}_{-0.07}$
	$\log N_{\rm H\,I}$	Y	Column density of neutral hydrogen	$\mathcal{U}(17, 25)$	$21.96^{+0.08}_{-0.09}$ (±0.1)
Other	$j_{\rm spec}$	Y	Multiplicative noise inflation term for spectrum	$\mathcal{U}(0.5, 2)$	$1.5^{+0.3}_{-0.4}$
	$\log {\rm SFR}_{10}[{\rm M}_\odot\,{\rm yr}^{-1}\,\mu^{-1}]$ (†)	N	SFR averaged over the last 10 Myr	–	$1.16^{+0.05}_{-0.07}$ (±0.05)
	$\log {\rm SFR}_{100}[{\rm M}_\odot\,{\rm yr}^{-1}\,\mu^{-1}]$ (†)	N	SFR averaged over the last 100 Myr	–	$0.29^{+0.14}_{-0.09}$(±0.1)
	$A_{\rm v}$[mag]	N	Optical dust attenuation	–	$0.19^{+0.07}_{-0.05}$(±0.05)
	$F_{\rm [O\,III]}[10^{-19}\,{\rm erg\,s^{-1}\,cm^{-2}}]$	N	FIR [O III]line flux	–	$2.77^{+0.79}_{-0.78}$(±0.05)
	Age [Myr]	N	Mass-weighted stellar age	–	40 ± 5

Notes. (1) Parameter name and units (where applicable). (2) Only parameters marked with 'Y' are optimized by `prospector`; parameters marked with 'N' are either tied to other parameters (see Column 4), or are calculated after the fit from the posterior distribution (in this case, Column 4 is empty). (3) Parameter description. (4) Parameter prior probability distribution; $\mathcal{N}(\mu, \sigma)$ is the normal distribution with mean μ and dispersion σ; $\mathcal{U}(a, b)$ is the uniform distribution between a and b; $\mathcal{T}(\mu, \sigma, \nu)$ is the Student's t distribution with mean μ, dispersion σ and ν degrees of freedom; $\mathcal{G}(\mu, \sigma; a, b)$ is the normal distribution with mean μ and dispersion σ, truncated between a and b. (5) Median and 16$^{\rm th}$–84$^{\rm th}$ percentile range of the marginalised posterior distribution; for some nuisance parameters we do not present the posterior statistics (e.g., log SFR ratios). (†)We corrected all extensive quantities for gravitational lensing, using $\mu = 1.17$ (Carniani et al. 2024). (‡)The non-parametric SFH is expressed by the logarithm of the SFR between adjacent time bins; we use a 'rising' SFH probability prior, which at each time bin is a $\mathcal{T}$ distribution with mean log ratio $R(z) \equiv \log({\rm SFR}(z_i)/{\rm SFR}(z_{i+1}))$, where z_i is the redshift of the $i^{\rm th}$ SFH bin and the SFR(z) is given by Turner et al. (2025), their Eq. (4).

the posterior model (Fig. 5b). At the same time, the bright flux measured by MIRI requires a moderate contribution from the stellar continuum in addition to Hβ and [O III]$\lambda\lambda$4959, 5007. This stellar continuum displays a moderate Balmer break ($\approx$1.4, when measured without the nebular continuum). The ALMA line flux predicted by the model exhibits strong degeneracies with stellar mass, metallicity, SFR, and ionization parameter. These degeneracies highlight the power of combining ALMA and JWST observations to break parameter constraints and achieve a more comprehensive understanding of galaxy properties.

The SFH follows the rising shape of the prior probability, although we note that the prior width is significantly wider than the posterior probability (gray vs red shaded regions in Fig. 5f). We stress that the prior range shown in the SFH is the scale parameter of the Student's t distribution; the prior standard deviation is larger. The key constraints from the prior come at the earliest epochs, when the prior suppresses the earliest and least constrained stages of star formation. There is some indication of the SFH 'stalling' at recent times, with the SFR being roughly constant in the last 30 Myr. This goes against the rising expectation from the prior, which would give a certain degree of confidence to this stalling behavior. However, we also find that different assumptions on the dust attenuation and prior on the SFH do impact the exact shape of the recovered SFH.

5.2. Dynamical mass

Given that we spectroscopically resolve the emission line in the ALMA observations, we are now able to constrain the dynamical mass ($M_{\rm dyn}$), assuming that the system is close to virialization, and can compare it to the stellar mass from the `prospector` SED fitting. We estimated the dynamical mass following the approach described by Übler et al. (2023) using the equation:

$$M_{\rm dyn} = K(n)K(q)\frac{\sigma^2 R_e}{G} \quad (1)$$

where K(n) = 8.87 – 0.831n + 0.0241n^2 and with Sérsic index n, following Cappellari et al. (2006), K(q) = [0.87 + 0.38e$^{-3.71(1-q)}$]^2, with axis ratio q following van der Wel et al. (2022), σ is the integrated stellar velocity dispersion, and R_e is the effective radius. We remark that the above approach was calibrated for stellar kinematics of massive galaxies at $z = 0.8$ ($M_\star = 10^9$–10^{11} M$_\odot$). However, a range of possible calibrations (e.g., Wisnioski et al. 2018; Cappellari et al. 2013) provides similar answers, within 0.3 dex (see e.g. Marconcini et al. 2024). We use our measured value of σ = FHWM/2.355 = $43.5^{+12.3}_{-9.2}$ km s^{-1} from [O III]88 μm, to which we apply a correction of $\Delta\log(\sigma/({\rm km\ s^{-1}})) = +0.1$ following Übler et al. (2023), since galaxies with low integrated ionized gas velocity dispersion tend to have higher integrated stellar velocity dispersion (Bezanson et al. 2018). We adopt a R_e value of 260 ± 20 pc

from Carniani et al. (2024). For JADES-GS-z14-0, Helton et al. (2024) reports $n = 0.877 \pm 0.027$ for the Sérsic index and $q = 0.425 \pm 0.008$ for the axis ratio. However, since it is unclear whether the stellar emission in the rest-frame UV has the same morphological properties as the nebular emission in the rest-frame far-infrared, we adopt a range of values for the Sérsic index and axis ratio (n = 0.8–2 and q = 0.3–1). We thus estimate a $\log(M_{dyn}/M_\odot) = 9.0 \pm 0.2$.

This value of M_{dyn} is five times larger than the stellar mass from our SED fitting ($\log M_\star/M_\odot = 8.29^{+0.14}_{-0.09}$, which assumes a Chabrier 2003 IMF). Assuming a disc-like geometry with a mean inclination of $i = 60°$, this would imply a fraction of gas mass and dark matter in this galaxy of ∼80%. However, we stress that this gas mass fraction is an upper limit. If we adopt the stellar mass estimates inferred by Helton et al. (2024), who explored different star-formation histories, we infer a gas mass fraction lower than 50%–60%. Alternatively, if the inclination was very small (close to face on) or the [O III]extent is significantly broader than that of UV continuum emission, the line broadening could underestimate the dynamical mass. Observations with higher spatial resolution would be required to address this scenario.

6. A non-zero escape fraction?

The luminosity of the [O III]far-infrared line of JADES-GS-z14-0 indicates a gas-phase metallicity of about 0.2 $Z_\odot$, which is similar to that measured in other luminous galaxies such as GN-z11 (Bunker et al. 2024; Maiolino et al. 2024) and GHZ2 (Castellano et al. 2024; Zavala et al. 2024; Calabrò et al. 2024). Although these three galaxies have similar UV luminosities and metal enrichment conditions, most of the UV lines of JADES-GS-z14-0 are undetected in the deep NIRSpec observations. The upper limits on the rest-frame equivalent widths of JADES-GS-z14-0 are up to seven times lower with respect to those measured in GN-z11 and GHZ2.

A non-zero escape fraction of ionizing photons might explain the low intensity of UV emission lines in JADES-GS-z14-0. This scenario is also supported by the SED fitting of the combined ALMA and JWST datasets that report an escape fraction of at least 10%. Figure 6 shows the equivalent of C III] as a function of gas-phase metallicity from PROSPECTOR using exponential star-formation histories with stellar ages from 1 Myr to 50 Myr (see details in Appendix B. Independently from the stellar age, the EW of the UV line increases with decreasing metallicity down to 0.15 $Z_\odot$ and then decreases because carbon abundance decreases. To reproduce the strength of C III] of JADES-GS-z14-0, the gas phase metallicity should be either lower than 0.05 $Z_\odot$ or higher than 0.3 $Z_\odot$. The latter was considered less probable by Carniani et al. (2024) and Helton et al. (2024) because of the intensity of the MIRI flux and the stellar age of the galaxy. However, the new detection of the far-infrared oxygen line combined with the current SFR of the galaxy puts a stringent limit of 0.1–0.3 $Z_\odot$ to the gas-phase metallicity, which corresponds to the metallicity range excluded initially by the analysis based solely on the UV lines. With the new constraints from ALMA, PROSPECTOR thus requires an escape fraction of ∼10% to match the two apparently discordant observables of a relatively high [O III]flux but a relatively low EW of C III]. We stress that – like all SED fitting, we are assuming here a single-zone model, with a reference electron density and solar abundances (Byler et al. 2017).

The origin of such a high escape fraction can be the result of fast galactic outflows that expel gas to a large scale and carve the ISM of the galaxy. For example, Ferrara et al. (2025) predict that JADES-GS-z14-0 may have recently experienced a starburst phase and radiation-driven outflows have cleared the galaxy from dust and gas. Current JWST and ALMA data do not have the sensitivity to identify the presence of "wings" in the emission line profiles tracing outflowing gas. However, the analysis of the dynamical mass suggests that the potential well is dominated by the stellar population and a large fraction of the gas may have been removed from the galaxy. If the observed $\log(N_{HI}/cm^{-2}) = 22.23$ DLA described in Section 4.2 was a result of a potential galactic outflow, this would help explain its presence while also allowing for a high escape fraction of ionizing radiation. Another possible explanation is the ionizing photons escape along a different direction than that of DLA systems and are not absorbed (see Tacchella et al. 2024 for the $z = 5.94$ galaxy GS9422).

Intriguingly, the implied 10% escape fraction in a source with the luminosity of JADES-GS-z14-0 would imply the rapid formation of a local ionized 'bubble' allowing Lyα emission to escape through the intergalactic medium, as required for JADES-GS-z13-1-LA observed to have a bright Lyα line at $z = 13$ (Witstok et al. 2024).

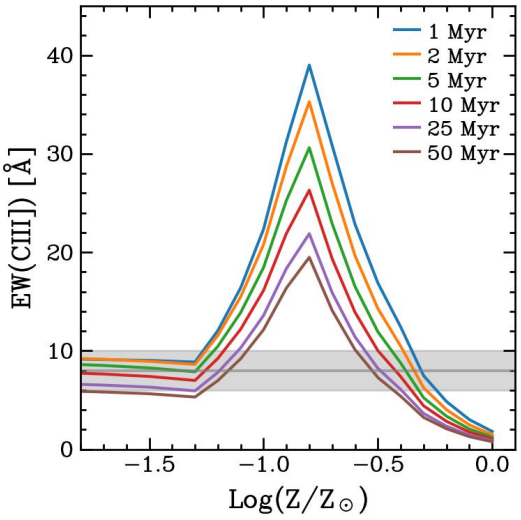

Fig. 6. EWs of C III] as a function of gas-phase metallicity. The blue, orange, green, red, purple, and brown curves denote the metallicity dependencies for exponential SFH (see Appendix B) with stellar ages of 1, 2, 5, 10, 25, and 50 Myr, respectively. The gray line and shaded region represent the C III] EW measurement of JADES-GS-z14-0. The observed C III] EW is typical of galaxies with $Z > 0.3\,Z_\odot$ or $Z < 0.05\,Z_\odot$

7. Carbon-to-oxygen abundance ratio

Leveraging the redshift delivered by the detection of [O III]88 µm in the ALMA observations, we can confirm the tentative detection of C III] previously reported by Carniani et al. (2024) in the JWST/NIRSpec spectrum at 2.89 µm. This allows us, under a number of fiducial assumptions discussed below, to derive the carbon-over-oxygen abundance (C/O) for JADES-GS-z14-0, yielding the most distant measurement of such abundance ratio to date.

To derive C/O, we first corrected the measured C III] flux for nebular attenuation assuming $A_V = 0.25$ as inferred from our SED modeling[2]. We then derive the C^{++}/O^{++} abundance from

[2] We used $A_V \equiv \tau_V \cdot (1 + \mu_d) \cdot 1.086$.

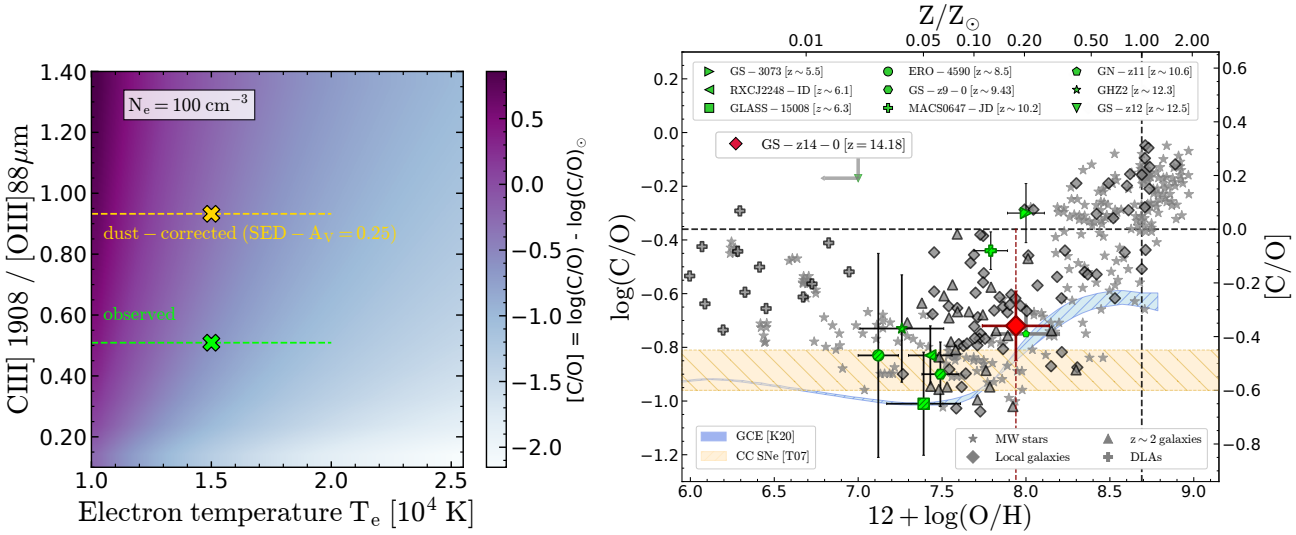

Fig. 7. Carbon-over-oxygen abundance for JADES-GS-z14-0. The left-hand panel shows how the final inferred C/O value changes as a function of the C III]/[O III]88 μm line ratio and of the electron temperature, T_e, under our fiducial assumption of N_e = 100 cm^{-3}. The observed and dust-corrected C III]/[O III]88 μm ratios for JADES-GS-z14-0 are marked in green and yellow, respectively. In the right-hand panel, we report our fiducial C/O measurement for JADES-GS-z14-0 on the C/O vs O/H diagram. The oxygen abundance is inferred from the best-fit PROSPECTOR metallicity reported in Table 2. The C/O value measured in JADES-GS-z14-0 is consistent with pure enrichment from core-collapse Supernovae. We also report for comparison a sample of C/O measurements from JWST compiled from the literature, namely GS-z12 (z = 12.5; D'Eugenio et al. 2024a), GHZ2 (z = 12.34; Castellano et al. 2024), GN-z11 (z = 10.6; Cameron et al. 2024), MACS0647-JD (z = 10.2; Hsiao et al. 2024b), GS-z9-0 (z = 9.4; Curti et al. 2025), ERO-4590 (z = 8.5; Arellano-Córdova et al. 2022), RXCJ2248-ID (z = 6.11; Topping et al. 2024), GLASS-150008 (z = 6.23; Jones et al. 2023), GS-3073 (z=5.5; Ji et al. 2024). The C/O vs O/H pattern predicted by Galactic Chemical Evolution models of Kobayashi et al. (2020) is shown in blue, whereas the C/O range allowed by the CC-SNe yields from Tominaga et al. (2007) is marked by the golden region.

the C III]/[O III]88 μm line ratio adopting PYNEB (Luridiana et al. 2015), assuming an electron temperature of T_e = 15 000 K and an electron density of n_e = 100 cm^{-3}. The assumed T_e value is consistent with the best-fit metallicity and ionization parameter inferred from the SED modeling, and we assume to reside in the low-density regime as suggested by the simultaneous modeling of the [O III]88 μm/[O III]5007 and [O III]5007/Hβ ratios (see Figure 4). We then correct the C^{++}/O^{++} abundance to the total C/O by applying an ionization correction factor (ICF) derived from the models presented in Berg et al. (2024), under the assumption of log(U) = −2.4 and Z = 0.2 $Z_\odot$ (i.e., the best-fit values from the SED fitting). The total C/O value is therefore log(C/O)= −0.72±0.13, corresponding to [C/O]=log(C/O)–log(C/O)$_\odot$ = –0.36, where the formal uncertainties are computed by randomly varying the measured fluxes by their errors and repeating the calculation 100 times, taking the standard deviation of the resulting C/O distribution.

Nonetheless, we note that variations in our assumptions on both T_e and n_e, as well as uncertainties associated with the dust attenuation correction, can have a non-negligible impact onto the final C/O. In the left panel of Figure 7, we show how the final inferred C/O value would change as a function of the C III]/[O III]88 μm line ratio (comparing in particular the observed and dust-corrected value based on the SED-inferred A_V) and of the electron temperature, under our fiducial assumption of n_e = 100 cm^{-3}. For instance, at fixed C III]/[O III]88 μm ratio and n_e, varying T_e between 15 000 K (our fiducial value) and 20 000K lowers the inferred C/O by ∼0.45 dex. On the other hand, assuming n_e = 300 cm^{-3} instead of 100 cm^{-3} (at fixed line ratio and T_e) would lower the C/O by ∼0.18 dex. We therefore estimate the amount of systematic uncertainty on our C/O derivation associated with different assumptions on density and temperature by computing the C/O values over a grid in n_e and T_e spanning $n_e \in [100,300]$ cm^{-3} and $T_e \in [10\,000, 20\,000]$ K, yielding a final log(C/O) = −0.72 ± 0.13 ($^{+0.3}_{-0.6}$ systematics).

In the right-panel of Figure 7, we finally plot JADES-GS-z14-0 on the C/O vs O/H diagram as the red diamond marker. The solid errorbars report the formal statistical uncertainty on C/O from the flux measurement errors (0.13 dex), whereas the dashed errorbars encompass the systematic uncertainties ($^{+0.3}_{-0.6}$) from our assumptions on n_e and T_e as discussed above. The oxygen abundance is inferred from the best-fit PROSPECTOR metallicity. For comparison, a compilation of C/O measurement at high-z from JWST spectroscopy is also shown (see the legend and caption of Figure 7 for details).

The fiducial C/O value measured in JADES-GS-z14-0 appears in line with expectations given its moderate metallicity, and it is consistent within the uncertainties with predictions from galactic chemical evolution models of the solar neighborhood (Kobayashi et al. 2020), as well as with the yields from pure core-collapse Supernovae (CC-SNe) enrichment (Tominaga et al. 2007), in agreement with a rapid and recent history of mass assembly. Nonetheless, we note that even slightly higher C/O values than predicted by pure CC-SNe enrichment, as possibly shown by taking our C/O measurement in JADES-GS-z14-0 at face value, might be indicative of a lower effective oxygen yield, as possibly driven by SNe-driven outflows preferentially expelling oxygen from the ISM following an intense phase of star-formation (as also discussed in Sect. 6), whereas any contribution to Carbon enrichment from evolved, low-mass stars is unlikely given the age of the system.

As a caveat, we reiterate that our C/O measurement assumes that C III] and [O III]88 μm trace regions with similar densities. However, the carbon line can originate from regions with densities exceeding the critical density of [O III]88 μm, potentially affecting the C/O abundance estimate. In the presence of multiple

density components, the C/O ratio can only be reliably measured using emission lines with comparable critical densities. In this context, deeper observations of JADES-GS-z14-0 with NIRSpec/JWST have the potential to detect O III]$\lambda\lambda$1661, 1666, which, when combined with C III], would enable a more precise determination of the carbon-to-oxygen ratio.

8. Conclusions

We have presented the analysis of the new DDT ALMA program targeting the [O III] 88 μm emission in the most distant and luminous galaxy known so far, JADES-GS-z14-0. We have detected the FIR line with a level of significance of 6.67σ at a frequency of 223.524 GHz. We have thus determined the spectroscopic redshifts of $z_{[OIII]} = 14.1796 \pm 0.0007$, in excellent agreement with that from the tentative detection of C III] ($z_{CIII]} = 14.178 \pm 0.013$), and consistent with the Lyman-break redshift ($z_{Ly\alpha} = 14.32^{+0.08}_{-0.20}$) when accounting for a DLA ($\log N_{H\,I}/cm^{-2} = 21.96^{+0.08}_{-0.09}$).

The measured luminosity of the line ($L_{[OIII]}/L_\odot = 8.3 \pm 0.1$) is consistent with the $L_{[OIII]}$ − SFR relation of local dwarf galaxies. The detection of the FIR line indicates a gas-phase metallicity $Z > 0.1\,Z_\odot$ and thus suggests a rapid metal enrichment during the earliest phases of galaxy formation. The modest metal enrichment measured in this work is somewhat unexpected, given the lack of most of the rest-frame UV emission lines in the deep NIRSpec spectrum (Carniani et al. 2024). However, the discrepancy between the two observations can be mitigated by assuming a non-zero escape fraction (∼10%), which would explain the low intensity of UV emission lines despite the modest gas-phase metallicity measured in JADES-GS-z14-0.

We have combined the MIRI flux at 7.7 μm and the ALMA detection to constrain the interstellar medium condition by using predictions from CLOUDY models. The excess of MIRI flux, likely associated to the nebular optical lines of oxygen and hydrogen, and the FIR $L_{[OIII]}$ set a stringent upper limit on the electron density of $n_e < 700\ cm^{-3}$ at $Z = 0.2\,Z_\odot$, which is lower than those previously found in several [OII]-emitting sources at $z > 9$ (e.g., Abdurro'uf et al. 2024; Marconcini et al. 2024; Zavala et al. 2024), and also lower compared to the average density ($n_e \sim 1000\ cm^{-3}$) expected at $z > 9$ from the extrapolation of the [OII]-derived n_e vs. z relation by Isobe et al. (2023). One possible physical reason is that galactic outflows may have expelled gas on large scales and reduced the gas density within the galaxy.

To constrain the properties of the stellar population and interstellar medium we have performed the SED fitting with PROSPECTOR to the JWST and ALMA data. The inferred star-formation rate and stellar mass are in agreement with those inferred by Carniani et al. (2024) and Helton et al. (2024). We note that PROSPECTOR results indicate a gas-phase metallicity 17% solar, but it requires an escape fraction of 0.1 to match the NIRSpec spectrum and, therefore, the weakness of the UV emission line. Combining the [O III]88 μm detection in ALMA with the 3.5σ C III] emission detected by JWST/NIRSpec, we also derive a carbon-over-oxygen abundance $\log(C/O) = -0.72 \pm 0.13\ (^{+0.3}_{-0.6})$, in agreement with chemical evolution models of the solar neighborhood given the moderate enrichment of the system.

We have spectroscopically resolved the [O III] allowing us to measure the dynamical mass of this galaxy of $\log(M_{dyn}) = 9.0 \pm 0.20$. We find this measurement consistent with the stellar mass estimated from PROSPECTOR, implying a gas fraction lower than 80%. However, we note that adopting different priors on the star formation history in the SED fitting process Helton et al. (2024) results in an inferred gas mass fraction below 50%–60%. We speculate that galactic outflows may have carved the interstellar medium, hence reducing the gas reservoir and resulting in a non-zero escape fraction as expected by PROSPECTOR results.

This study demonstrates that multi-wavelength observations are necessary to constrain the properties of galaxies at the highest redshifts. However, the detection of only one emission line is not sufficient to put stringent constraints on the interstellar medium condition. MIRI spectroscopic observations and deep NIRSpec data would allow us to investigate directly the luminosity of a range of optical and UV emission lines. Combined with ALMA, these lines would provide new insight on the metal enrichment conditions of the galaxy. Deeper and higher frequency ALMA observations capable of probing the dust continuum would also be invaluable, by providing crucial information on the dust content and attenuation.

Acknowledgements. This paper makes use of ALMA data: 2023.A.00037.S. ALMA is a partnership of ESO (representing its member states), NSF (USA) and NINS (Japan), together with NRC (Canada) and NSC and ASIAA (Taiwan), in cooperation with the Republic of Chile. The Joint ALMA Observatory is operated by ESO, AUI/NRAO and NAOJ. S.C, EP and GV acknowledge support from the European Union (ERC, WINGS,101040227). FDE, XJ, JS, RM and JW acknowledge support by the Science and Technology Facilities Council (STFC), ERC Advanced Grant 695671 "QUENCH" and the UKRI Frontier Research grant RISEandFALL. RM also acknowledges funding from UKRI Frontier Research grant RISEandFALL and a research professorship from the Royal Society. AJB and AS acknowledge funding from the "FirstGalaxies" Advanced Grant from the European Research Council (ERC) under the European Union's Horizon 2020 research and innovation programme (Grant agreement No. 789056). HÜ gratefully acknowledges support by the Isaac Newton Trust and by the Kavli Foundation through a Newton-Kavli Junior Fellowship. The authors acknowledge use of the lux supercomputer at UC Santa Cruz, funded by NSF MRI grant AST 1828315. CNAW and DJE are supported as a Simons Investigator and by JWST/NIRCam contract to the University of Arizona, NAS5-02015. The Cosmic Dawn Center (DAWN) is funded by the Danish National Research Foundation under grant DNRF140. BER and BDJ acknowledge support by JWST/NIRCam contract to the University of Arizona, NAS5-02015 and BDJ is supported by JWST Program 3215. The research of CCW is supported by NOIRLab, which is managed by the Association of Universities for Research in Astronomy (AURA) under a cooperative agreement with the National Science Foundation.

References

Abdurro'uf, Larson, R. L., Coe, D., et al. 2024, ApJ, 973, 47
Arellano-Córdova, K. Z., Berg, D. A., Chisholm, J., et al. 2022, ApJ, 940, L23
Arrabal Haro, P., Dickinson, M., Finkelstein, S. L., et al. 2023, Nature, 622, 707
Berg, D. A., Skillman, E. D., Chisholm, J., et al. 2024, ApJ, 971, 87
Bezanson, R., van der Wel, A., Straatman, C., et al. 2018, ApJ, 868, L36
Bunker, A. J., Saxena, A., Cameron, A. J., et al. 2023, A&A, 677, A88
Bunker, A. J., Cameron, A. J., Curtis-Lake, E., et al. 2024, A&A, 690, A288
Byler, N., Dalcanton, J. J., Conroy, C., & Johnson, B. D. 2017, ApJ, 840, 44
Byrne, C. M., Stanway, E. R., Eldridge, J. J., McSwiney, L., & Townsend, O. T. 2022, MNRAS, 512, 5329
Calabrò, A., Castellano, M., Zavala, J. A., et al. 2024, ApJ, 975, 245
Cameron, A. J., Katz, H., Witten, C., et al. 2024, MNRAS, 534, 523
Cappellari, M., Bacon, R., Bureau, M., et al. 2006, MNRAS, 366, 1126
Cappellari, M., Scott, N., Alatalo, K., et al. 2013, MNRAS, 432, 1709
Carilli, C. L., & Walter, F. 2013, ARA&A, 51, 105
Carniani, S., Maiolino, R., Pallottini, A., et al. 2017, A&A, 605, A42
Carniani, S., Gallerani, S., Vallini, L., et al. 2019, MNRAS, 489, 3939
Carniani, S., Ferrara, A., Maiolino, R., et al. 2020, MNRAS, 499, 5136
Carniani, S., Hainline, K., D'Eugenio, F., et al. 2024, Nature, 633, 318
Castellano, M., Napolitano, L., Fontana, A., et al. 2024, ApJ, 972, 143
Chabrier, G. 2003, PASP, 115, 763
Choi, J., Dotter, A., Conroy, C., et al. 2016, ApJ, 823, 102
Conroy, C., & Gunn, J. E. 2010, ApJ, 712, 833
Conroy, C., Gunn, J. E., & White, M. 2009, ApJ, 699, 486
Conroy, C., Naidu, R. P., Zaritsky, D., et al. 2019, ApJ, 887, 237
Cowie, L. L., & Songaila, A. 1986, ARA&A, 24, 499
Curti, M., Witstok, J., Jakobsen, P., et al. 2025, A&A, in press, https://doi.org/10.1051/0004-6361/202451410

Curtis-Lake, E., Carniani, S., Cameron, A., et al. 2023, Nat. Astron., 7, 622
da Cunha, E., Groves, B., Walter, F., et al. 2013, ApJ, 766, 13
Davies, R. L., Förster Schreiber, N. M., Genzel, R., et al. 2021, ApJ, 909, 78
Dekel, A., Sarkar, K. C., Birnboim, Y., Mandelker, N., & Li, Z. 2023, MNRAS, 523, 3201
De Looze, I., Cormier, D., Lebouteiller, V., et al. 2014, A&A, 568, A62
Dere, K. P., Landi, E., Mason, H. E., Monsignori Fossi, B. C., & Young, P. R. 1997, A&AS, 125, 149
D'Eugenio, F., Maiolino, R., Carniani, S., et al. 2024a, A&A, 689, A152
D'Eugenio, F., Cameron, A. J., Scholtz, J., et al. 2024b, ArXiv e-prints [arXiv:2404.06531]
Donnan, C. T., McLure, R. J., Dunlop, J. S., et al. 2024, MNRAS, 533, 3222
Dopita, M. A., Kewley, L. J., Heisler, C. A., & Sutherland, R. S. 2000, ApJ, 542, 224
Eldridge, J. J., Stanway, E. R., Xiao, L., et al. 2017, PASA, 34
Ferland, G. J., Chatzikos, M., Guzmán, F., et al. 2017, Rev. Mex. Astron. Astrofis., 53, 385
Ferrara, A. 2024, A&A, 684, A207
Ferrara, A., Pallottini, A., & Dayal, P. 2023, MNRAS, 522, 3986
Ferrara, A., Carniani, S., di Mascia, F., et al. 2025, A&A, 694, A215
Finkelstein, S. L., Bagley, M. B., Ferguson, H. C., et al. 2023, ApJ, 946, L13
Fujimoto, S., Ouchi, M., Nakajima, K., et al. 2024, ApJ, 964, 146
Gordon, K. D., Clayton, G. C., Misselt, K. A., Landolt, A. U., & Wolff, M. J. 2003, ApJ, 594, 279
Grevesse, N., Asplund, M., Sauval, A. J., & Scott, P. 2010, Ap&SS, 328, 179
Groves, B. A., Dopita, M. A., & Sutherland, R. S. 2004, ApJS, 153, 9
Hainline, K. N., Johnson, B. D., Robertson, B., et al. 2024a, ApJ, 964, 71
Hainline, K. N., D'Eugenio, F., Jakobsen, P., et al. 2024b ArXiv e-prints [arXiv:2404.04325]
Harikane, Y., Ouchi, M., Inoue, A. K., et al. 2020, ApJ, 896, 93
Hegde, S., Wyatt, M. M., & Furlanetto, S. R. 2024, JCAP, 2024, 025
Heintz, K. E., Watson, D., Brammer, G., et al. 2024, Science, 384, 890
Heintz, K. E., Brammer, G. B., Watson, D., et al. 2025, A&A, 693, A60
Helton, J. M., Rieke, G. H., Alberts, S., et al. 2024, ArXiv e-prints [arXiv:2405.18462]
Hsiao, T. Y. Y., Abdurro'uf, Coe, D., et al. 2024a, ApJ, 973, 8
Hsiao, T. Y. Y., Topping, M. W., Coe, D., et al. 2024b, ArXiv e-prints [arXiv:2409.04625]
Inayoshi, K., Harikane, Y., Inoue, A. K., Li, W., & Ho, L. C. 2022, ApJ, 938, L10
Isobe, Y., Ouchi, M., Nakajima, K., et al. 2023, ApJ, 956, 139
James, B. L., Pettini, M., Christensen, L., et al. 2014, MNRAS, 440, 1794
Jenkins, E. B. 1987, in Interstellar Processes, eds. D. J. Hollenbach, & H. A. Thronson, Astrophys. Space Sci. Libr., 134, 533
Ji, X., Maiolino, R., Ferland, G., et al. 2024, ArXiv e-prints [arXiv:2405.05772]
Johnson, B. D., Leja, J., Conroy, C., & Speagle, J. S. 2021, ApJS, 254, 22
Jones, T., Sanders, R., Roberts-Borsani, G., et al. 2020, ApJ, 903, 150
Jones, T., Sanders, R., Chen, Y., et al. 2023, ApJ, 951, L17
Kashino, D., Silverman, J. D., Sanders, D., et al. 2017, ApJ, 835, 88
Katz, H., Cameron, A. J., Saxena, A., et al. 2024, ArXiv e-prints [arXiv:2408.03189]
Kobayashi, C., Karakas, A. I., & Lugaro, M. 2020, ApJ, 900, 179
Koposov, S., Speagle, J., Barbary, K., et al. 2022, https://doi.org/10.5281/zenodo.7388523
Kriek, M., & Conroy, C. 2013, ApJ, 775, L16
Landi, E., Young, P. R., Dere, K. P., Del Zanna, G., & Mason, H. E. 2013, ApJ, 763, 86
Leja, J., Carnall, A. C., Johnson, B. D., Conroy, C., & Speagle, J. S. 2019, ApJ, 876, 3
Luridiana, V., Morisset, C., & Shaw, R. A. 2015, A&A, 573, A42
Maiolino, R., Carniani, S., Fontana, A., et al. 2015, MNRAS, 452, 54
Maiolino, R., Scholtz, J., Witstok, J., et al. 2024, Nature, 627, 59
Marconcini, C., D'Eugenio, F., Maiolino, R., et al. 2024, MNRAS, 533, 2488
Mason, C. A., Trenti, M., & Treu, T. 2023, MNRAS, 521, 497
McMullin, J. P., Waters, B., Schiebel, D., Young, W., & Golap, K. 2007, in Astronomical Data Analysis Software and Systems XVI, eds. R. A. Shaw, F. Hill, & D. J. Bell, ASP Conf. Ser., 376, 127
Mingozzi, M., James, B. L., Arellano-Córdova, K. Z., et al. 2022, ApJ, 939, 110
Mirocha, J., & Furlanetto, S. R. 2023, MNRAS, 519, 843
Robertson, B. E., Tacchella, S., Johnson, B. D., et al. 2023, Nat. Astron., 7, 611
Robertson, B., Johnson, B. D., Tacchella, S., et al. 2024, ApJ, 970, 31
Sanders, R. L., Shapley, A. E., Kriek, M., et al. 2016, ApJ, 816, 23
Sanders, R. L., Shapley, A. E., Topping, M. W., Reddy, N. A., & Brammer, G. B. 2024, ApJ, 962, 24
Schneider, R., & Maiolino, R. 2024, A&ARv, 32, 2
Shen, X., Vogelsberger, M., Boylan-Kolchin, M., Tacchella, S., & Kannan, R. 2023, MNRAS, 525, 3254
Speagle, J. S. 2020, MNRAS, 493, 3132
Spitzer, L. J., & Greenstein, J. L. 1951, ApJ, 114, 407
Stanway, E. R., & Eldridge, J. J. 2018, MNRAS, 479, 75
Strom, A. L., Steidel, C. C., Rudie, G. C., et al. 2017, ApJ, 836, 164
Tacchella, S., Bose, S., Conroy, C., Eisenstein, D. J., & Johnson, B. D. 2018, ApJ, 868, 92
Tacchella, S., Finkelstein, S. L., Bagley, M., et al. 2022a, ApJ, 927, 170
Tacchella, S., Conroy, C., Faber, S. M., et al. 2022b, ApJ, 926, 134
Tacchella, S., Eisenstein, D. J., Hainline, K., et al. 2023, ApJ, 952, 74
Tacchella, S., McClymont, W., Scholtz, J., et al. 2024, ArXiv e-prints [arXiv:2404.02194]
Tominaga, N., Umeda, H., & Nomoto, K. 2007, ApJ, 660, 516
Topping, M. W., Stark, D. P., Endsley, R., et al. 2024, MNRAS, 529, 4087
Trinca, A., Schneider, R., Valiante, R., et al. 2024, MNRAS, 529, 3563
Turner, C., Tacchella, S., D'Eugenio, F., et al. 2025, MNRAS, 537, 1826
Übler, H., Maiolino, R., Curtis-Lake, E., et al. 2023, A&A, 677, A145
Umeda, H., Ouchi, M., Nakajima, K., et al. 2024, ApJ, 971, 124
van der Wel, A., van Houdt, J., Bezanson, R., et al. 2022, ApJ, 936, 9
Virtanen, P., Gommers, R., Oliphant, T. E., et al. 2020, Nat. Methods, 17, 261
Wang, B., Fujimoto, S., Labbé, I., et al. 2023, ApJ, 957, L34
Whitler, L., Stark, D. P., Endsley, R., et al. 2023, MNRAS, 519, 5859
Wilkins, S. M., Lovell, C. C., Vijayan, A. P., et al. 2023, MNRAS, 522, 4014
Wisnioski, E., Mendel, J. T., Förster Schreiber, N. M., et al. 2018, ApJ, 855, 97
Witstok, J., Smit, R., Maiolino, R., et al. 2022, MNRAS, 515, 1751
Witstok, J., Jones, G. C., Maiolino, R., Smit, R., & Schneider, R. 2023, MNRAS, 523, 3119
Witstok, J., Jakobsen, P., Maiolino, R., et al. 2024, ArXiv e-prints [arXiv:2408.16608]
Zavala, J. A., Castellano, M., Akins, H. B., et al. 2024, ArXiv e-prints [arXiv:2403.10491]

Appendix A: fidelity of ALMA [O III] line detection

To assess the fidelity of ALMA [O III] 88 μm line detection at 223.524 GHz, we have blindly searched for positive and negative peaks in reduced ALMA spectral cube. Using the natural cube, we first measure noise spectrum from each channel (median: 0.15 mJy beam^{-1} per 10 km s^{-1} velocity bin). We then bin the spectral cube with various velocity sizes of 30, 50, ..., 170 km s^{-1}, respectively, and search for positive and negative peaks in the collapsed spectral cubes over the central 25″ × 25″ region. The S/N of detected peaks is computed by the peak brightness divided by the noise spectrum collapsed over the same velocity bin.

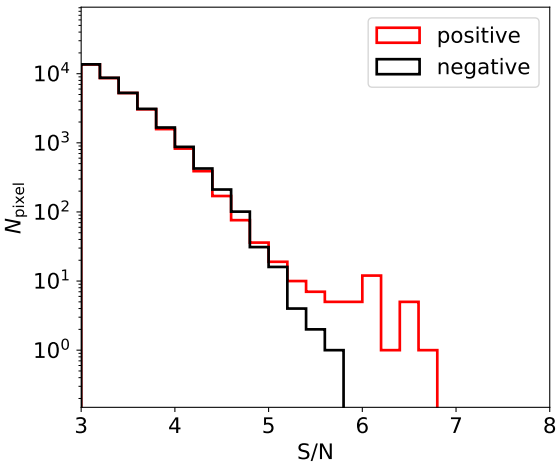

Fig. A.1. Statistics of positive and negative peaks from natural-weighted spectral cubes, collapsed with various velocity bin sizes at 30–170 km s^{-1}. The maximum S/N = 6.67 is seen at the centroid of JADES-GS-z14-0 at 223.524 GHz with a velocity bin size of 130 km s^{-1}, for which we interpret as an [O III] 88 μm line detection at z = 14.1796. This is much more significant than the strongest negative peak seen in the spectral cube (-5.7σ). Therefore, we conclude the fidelity of ALMA line detection.

Figure A.1 summarizes the statistics of positive and negative peaks throughout the collapsed spectral cubes. The maximum S/N of the collapsed spectral cubes is seen at the centroid of JADES-GS-z14-0 with a velocity bin size of 130 km s^{-1} at a central frequency of 223.524 GHz, for which we interpret as an [O III] 88μm emission line detection at z = 14.1796 ± 0.0007. We also examine the noise spectrum and conclude no additional telluric absorption or contamination is present at this frequency. This line detection is much more significant than the strongest negative peak seen within the spectral cube, which is at S/N = –5.73 with velocity bin size of 50 km s^{-1}. We have also experimented the Briggs-weighted (robust=0.5) spectral cube and the conclusion is similar, although the line S/N is slightly reduced to 6.22. The reduced S/N in Briggs-weighted cube with smaller synthesized beam size may indicate that the [O III] 88 μm line of JADES-GS-z14-0 is spatially extended. Although this is consistent with the spatially extended nature of JADES-GS-z14-0 in the rest-frame UV, the current line S/N is not high enough to ensure a robust size measurement of [O III] 88 μm emission. Nevertheless, we conclude the fidelity of the ALMA emission line presented in this work.

Appendix B: balmer break

Helton et al. (2024) determine that at least one-third of the flux detected with the MIRI filter 770W comes from the rest-frame optical emission lines Hβ and optical [O III]doublet. However, determining the intensity of these optical nebular lines requires follow-up MIRI observations in Low-Resolution Spectroscopy mode to disentangle the continuum emission from the line emission component. Indeed. the excess flux of 27.5 nJy in F770W with respect to F444W (Helton et al. 2024) is not a direct measurement of the Hβ +[O III]line intensity as the flux level of the underlining continuum emission at 7.7μm might be different from that measured in the F444W filter. The Balmer break, which is the ratio between the continuum emission at $\lambda_{\rm rest}$ = 4200 Å and that at $\lambda_{\rm rest}$ = 3500 Å depends mainly on the stellar age. Wilkins et al. (2023) shows that the luminosity ratio $\log_{10}(L_{4200}/L_{3500})$ is as large as -0.3 for a stellar population with a stellar age of 1 Myr and reaches a value of about 0.5 for a galaxy with an average stellar age of 1 Gyr. The authors also emphasized that the strength of the Balmer break is also influenced by the shape of the star-formation history.

To constrain the intensity of the optical Hβ +[O III]line of JADES-GS-z14-0, we have evaluated the dependence of the continuum emission at 7.7 μm on the star-formation history. In particular, we have assumed five different exponential star-formation histories of the form $SFR(t) \propto \exp^{-t/\tau}$ where t corresponds to the time before the observations (i.e, lookback time) and τ has been selected to return mass-weighted stellar ages of 1, 5, 10, 25, and 50 Myrs (Fig. B.1). We have generated a mock galaxy spectrum for each star-formation history by using BPASS models Eldridge et al. (2017), Stanway & Eldridge (2018), Byrne et al. (2022) for the stellar population and the nebular line and continuum component with CLOUDY. We have then normalized the spectra to the photometric value 46.9nJy, calculated within the wavelength range covered by the NIRCam F444W filter Robertson et al. (2023), Helton et al. (2024), Carniani et al. (2024). Finally, we have removed the emission line from the spectra and estimated the flux density in the MIRI filter F770W. The bottom panel of Fig. B.1 illustrates the flux density in the MIRI filter with respect to the NIRCam flux density at 4.5 μm. We note that the two flux densities are comparable when the mass-weighted stellar age of the galaxy is larger than 40-50 Myrs. In the extreme case where the mass-weighted stellar ages are of the order of 1 Myr, the continuum flux density level in the MIRI filter is about 0.65 times lower than that measured in the NIRCam wavelength range. In this case, the equivalent width of the nebular optical lines can be higher than that estimated assuming that the continuum flux level at 7.7 μm is as large as the continuum at 4.5 μm.

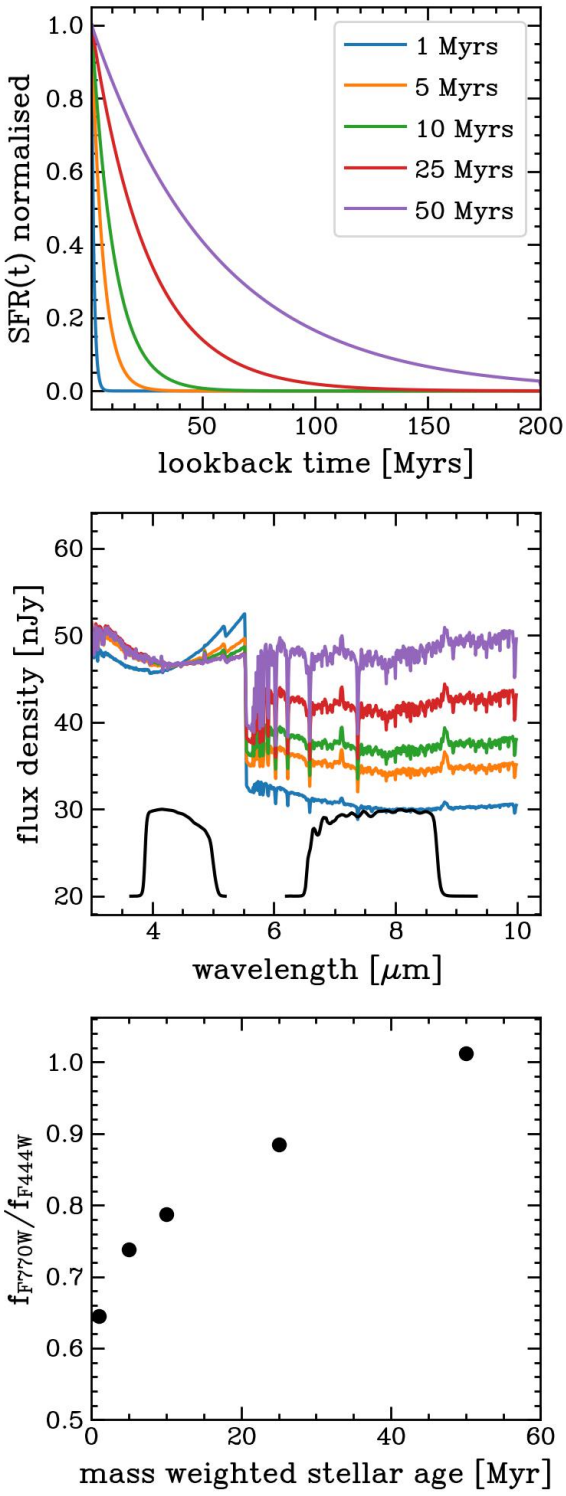

Fig. B.1. Top: star-formation histories (SFHs) with different mass-weighted stellar age and of the form $SFR(t) \propto \exp^{-t/\tau}$. The line colors correspond to the stellar age reported in the legends Middle: SED models after removing emission lines for each SFHs and color-coded depending on the stellar age reported in the top panel. All SEDs are normalized to the flux density level of 46.9 nJy in the NIRCam F444W filter. The black lines show the transmission curves for F444W (left) and F770W (right) JWST filters. Bottom: flux density ratio between the F770W and F444W filters as a function of the mass-weighted stellar age.